Aalto University
School of Electrical
Engineering

Master's Programme in Space Science and Technology

Modelling and Design of a Control System for a Laser Communication System on UAV Platforms

Nico Kujanen

Master's Thesis
2024

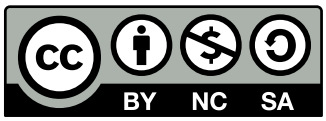

Aalto University
School of Electrical
Engineering

Author Nico Kujanen

Title Modelling and Design of a Control System for a Laser Communication System on UAV Platforms

Degree programme Space Science and Technology

Major Space Robotics and Automation

Supervisor Prof. Dominik Baumann

Advisors Dr. Carlos Carrizo, Dr. Markus Knapek

Collaborative partner Cucuyo GmbH

Date 31 July 2024 **Number of pages** 48 **Language** English

Abstract

This thesis presents the modelling and design of a control system for a laser communication terminal on UAV platforms. It was written in collaboration with Cucuyo GmbH, whose P-100 terminal is used for the experimental work. However, the chosen methods can also be applied to similar systems that employ 2-axis gimbals and beam steering mirrors. This thesis explores different modeling approaches for control design and discusses their limitations when applied to real systems. Frequency response analysis is performed on the coarse pointing assembly to design a suitable PI controller and filter combination to ensure stability in varying conditions. The combined dynamics of the coarse pointing assembly and the fine pointing assembly are compared against expected platform disturbances to verify that the system can reach the set performance goals. Possible improvements to the P-100 terminal and the control system design procedure are also discussed.

Keywords control system, laser communication, UAV, PI, PID, CPA, FPA, controller, frequency response, sensitivity function, gimbal

Aalto-yliopisto
Sähkötekniikan
korkeakoulu

Tekijä Nico Kujanen

Työn nimi Säätöjärjestelmän mallintaminen ja suunnittelu miehittämättömien ilma-aluksien laserkommunikaatiojärjestelmälle

Koulutusohjelma Space Science and Technology

Pääaine Space Robotics and Automation

Työn valvoja Prof. Dominik Baumann

Työn ohjaajat Dr. Carlos Carrizo, Dr. Markus Knapek

Yhteistyötaho Cucuyo GmbH

Päivämäärä 31.7.2024 **Sivumäärä** 48 **Kieli** englanti

Tiivistelmä

Tässä työssä suunniteltiin ja mallinnettiin säätöjärjestelmä miehittämättömiin ilma-aluksiin tarkoitettua laserkommunikaatiojärjestelmää varten. Tämä työ on kirjoitettu yhteistyössä Cucuyo GmbH kanssa. Cucuyo GmbH on Saksassa toimiva start-up, jonka P-100 laserkommunikaatiojärjestelmä on työn käytännön osuuden keskiössä. Siitä huolimatta työssä käytettyjä menetelmiä voi soveltaa myös muihin järjestelmiin, jotka hyödyntävät kahden vapausasteen vakaajia ja jännitteellä ohjattavia peilejä lasersäteiden suuntaamiseen. Tässä työssä tutkitaan eri mallintamismenetelmiä ja niiden rajoituksia oikeita järjestelmiä mallinnettaessa. Karkean suuntausjärjestelmän (engl. coarse pointing assembly) taajuusvaste mitataan ja sitä hyödynnetään sopivan PI säätimen ja suodattimen suunnittelussa. Karkean suuntausjärjestelmän ja hienosuuntaimen (engl. fine pointing assembly) yhdistettyä vastetta verrataan oletettuihin ilma-aluksen tuottamiin häiriöihin, jotta voidaan varmistaa säätimen ja yhdistetyn järjestelmän toimivuus suunnitellussa käyttöympäristössä. Työn lopussa käydään läpi myös mahdolliset parannusehdotukset P-100 laserkommunikaatiojärjestelmään, ja säätöjärjestelmän suunnittelumenetelmän toimivuutta arvioidaan.

Avainsanat Säätöjärjestelmä, ohjausjärjestelmä, PI säädin, laserkommunikaatio, ilma-alus, taajuusvaste, taajuusanalyysi, gimbal

Preface

I want to thank my thesis supervisor Professor Dominik Baumann and my advisors Dr. Carlos Carrizo and Dr. Markus Knapek for their guidance throughout the thesis process. I also want to thank everyone else at Cucuyo GmbH for the support.

I also want to thank Anshuman for keeping me sane and alive.

Espoo, 31 July 2024

Nico Kujanen

Contents

Symbols and abbreviations

Symbols

V	Voltage
L	Inductance
I	Current
R	Resistance
e_b	Back electromotive force
K	Motor constant
ω	Angular velocity
J	Moment of inertia
T	Torque
t	Time
B	Viscous friction coefficient
s	Complex frequency
$H(s)$	Transfer function notation
$\mathbf{x}$	State vector
$\mathbf{y}$	Output vector
$\mathbf{u}$	Input vector
$\mathbf{A}$	State matrix
$\mathbf{B}$	Input matrix
$\mathbf{C}$	Output matrix
$\mathbf{D}$	Feedthrough matrix

Abbreviations

4QD	Four quadrant detector
APD	Avalanche photodiode
BLDC	Brushless direct current
CBS	Chromatic beam splitter
CPA	Coarse pointing assembly
DC	Direct current
EASII	Elmo Application Studio II
EMF	Electromotive force
FPA	Fine pointing assembly
GNSS	Global navigation satellite system
GS	Ground station
MEMS	Micro electromechanical system
MIMO	Multiple input multiple output
NBSC	Neutral beam splitter cube
OCT	Optical communication terminal
OGS	Optical ground station
PAT	Pointing, acquisition and tracking
RF	Radio frequency
SISO	Single input single output
TLA	Telescope assembly
UAV	Unmanned aerial vehicle
WP	Waypoint

1 Introduction

Recent years have seen an increase in popularity of unmanned aerial vehicles (UAVs) in both civilian and military use. UAVs can be used to operate in environments where human operation would be deemed challenging or dangerous, which makes them a valuable tool for various applications such as surveillance, reconnaissance, disaster management, monitoring of critical infrastructure, and aerial photography to name a few [1, 2, 3]. For these operations to be successful, the UAV must be able to communicate with the ground station or other UAVs in a quick, stable and secure manner. Traditionally, radio frequency (RF) communications have been used for UAV communications, but they can face problems such as bandwidth limitations and electronic interference [4]. These problems can be overcome with laser communication systems, which generally offer higher data transfer rates and do it more securely, due to the narrow beamwidth which also cannot be intercepted inconspicuously.

Laser communications have long been used in space applications [5] and more recently also in UAV platforms. Counterintuitively, using laser communications in space environment is generally less complex than on Earth as the spacecraft is more stable a platform and most of the time the beam travels in free space. Although a considerable amount of research has been dedicated to laser communications on moving platforms, a great deal of it is focused on space communications, particularly on constellations and interconnected satellite networks such as Starlink, Project Kuiper, and the Kepler Network. On earth, the optical signals and the UAV platforms are subjected to atmospheric perturbations, which can directly affect the signal quality through changes in the optical medium or the pointing accuracy through platform vibrations [6]. Little can be done to react to the dynamic changes in the medium, but the platform vibrations can be corrected by actuators that counteract the movements of the platform. Usually, the stabilisation system is divided into the coarse-pointing assembly (CPA) and the fine-pointing assembly (FPA). The CPA is used to correct high amplitude and low frequency disturbances, whereas the FPA is used to correct low amplitude and high frequency disturbances. Most often the CPA is a 2-axis gimbal actuated by brushless DC (BLDC) motors. The FPA can be a smaller inner gimbal or most of the time an electrically controlled mirror that is used to steer the beam [7]. It is safe to say that the dynamics between the CPA and the FPA play an important role in the overall performance of the stabilisation system, and one should not be designed without keeping in mind the other. Even though many papers have been published on CPA and FPA design, particularly on 2-axis gimbals [8, 9, 10], many of them do not consider the effects of the combined dynamics.

The aim of this thesis is to create a model of the CPA and to design a control system for it. The process should be reproducible and it should be possible to implement it on other similar systems. The model should capture the essential system dynamics and the control system should achieve pointing, acquisition, tracking, and stabilisation of the optical signal with minimal tracking error. The CPA should also be able to offload the FPA every time it drifts away from its centre position. The mathematical model of the CPA will be based on the input-output measurements on both of its axes. The controller design will be based on this mathematical model and the simulated

combined system dynamics. The scope of the thesis does not extend to the FPA, but the combined dynamics must be considered when designing the controller for the CPA. Lastly, the design is for existing hardware, which sets some limitations and requirements for the system. The rest of the thesis is structured as follows. Chapter 2 reviews recent developments in the field to gain understanding of the research problem and existing solutions. Chapter 3 introduces the system concept and design. Chapter 4 specifies the system boundaries and the scope of the model. Chapter 5 builds the theoretical framework by introducing relevant concepts in system modelling and controller design. Chapter 6 presents the practical work of the thesis and applies the concepts introduced in chapter 5. This includes system identification, model fitting, and controller design. Chapter 7 evaluates the results obtained in chapter 6. This includes model verification, controller testing and discussion on the CPA-FPA integration. Chapter 8 concludes the thesis by summarising the work, evaluating the overall results and providing suggestions for future work.

2 Recent developments

This section discusses recent publications in the field of UAV laser communications and presents the relevant results and trends. The first subsection focuses on laser communications on UAV platforms and introduces the commonly used stabilisation subsystems. The second subsection explores the various controller designs for the stabilisation systems found in literature.

2.1 Laser communications on UAV platforms

Laser communication systems have long been used in space applications, particularly in satellite constellations. Due to the demand for higher data rates and more secure communications, laser communication systems are becoming a compelling alternative to the more traditional RF systems. Major projects like Starlink and Project Kuiper, alongside specialised companies such as TESAT and Mynaric, are pushing the development of laser communications forward.

With the increasing popularity of UAVs, more research has also been made on the subject. The two major challenges in terrestrial free-space laser communication are the atmospheric effects and beam alignment errors, the latter of which will be the focus of this thesis. Laser communications require high precision alignment to be able to form stable communication links, and to achieve this on stable platforms, a stabilisation system is required. According to Hilkert, one of the main components of inertially stabilised platforms usually is a gimbal [7]. A gimbal in this context refers to a device or a motor that allows the attached load to maintain its orientation regardless of the movement of the surrounding frame. These kinds of gimbal systems are indeed a common way to achieve stabilisation [11, 8] and they are often the stabilisation method of choice for UAV platforms [10, 12, 13, 14].

The 2-axis gimbal is often used to perform the coarse stabilisation. The fine stabilisation can be achieved with many different ways. Some of the systems implement a smaller inner gimbal to correct the higher frequency disturbances [13] but the most common method by far is to use a small electrically controlled mirror, usually a micro electromechanical system (MEMS) mirror, that can be used to steer the laser beam inside the optical system [10, 14].

Current inertially stabilising systems on UAV platforms seem to favour 2-axis gimbals for coarse stabilisation and fast steering mirrors (FSM) for fine stabilisation. The system examined in this thesis also employs a 2-axis gimbal paired with a MEMS mirror for fine stabilisation. In the next subsection some common control strategies for the stabilisation systems are reviewed.

2.2 Controller design for gimbal systems

For a gimbal system to achieve stabilisation, it must be able to react to outside disturbances. This is done by implementing a controller that will measure the platform rotations and send appropriate control signals to the motors responsible for maintaining the orientation. The most widely used controller type is a PID controller [15]. The

popularity is explained by its good performance and more importantly the ease of implementation.

Even though PID based controllers are still widely used, a lot of research is done on experimental control techniques. Some of these control strategies are still based on the PID control. For instance, Duan et al. investigate a a gimbal controller that is based on a PID type-III control scheme, which adds a second derivative term to the regular PID controller. Even when the controllers are not based on the PID logic, it is often used as a benchmark in studies. Shen et al. are developing a disturbance observer method with modelled dynamics, and report an increase of 90% in disturbance suppression compared to the traditional PID control [13]. Many control designs are also based on the H infinity methods [16, 10, 17]. A general predictive control (GPC) model is also proposed by Pirzadeh and Toloei [12] and the performance is compared to a PI controller.

Many research papers have been dedicated to finding optimal control strategies for gimbal systems. Some of the results are very promising and the proposed models offer increased disturbance rejection capabilities compared to the traditional PID control schemes. However, this thesis will mainly focus on PID control as the system used in the thesis is still in the prototyping phase and the PID control has been researched extensively and it is easy to implement.

3 System concept and design

This section reviews the overall design and concept of the laser communication terminal studied in the thesis. The first subsection introduces the collaborative partner and the company responsible for the development of the terminal. The second subsection begins by describing the operating principles of the laser communications terminal and what a typical UAV mission utilizing the terminal would look like. It also presents the performance requirements and necessary features of the terminal. The second subsection concludes with a description of the overall design of the terminal and how it helps to achieve the performance metrics stated earlier. The FPA and the optical design are discussed briefly to gain a better understanding of the system, but the main focus is in the electromechanical design of the CPA.

3.1 Cucuyo GmbH

This thesis was written in collaboration with Cucuyo GmbH, a technology start-up based in Krailling, Germany. The company focuses on the development of commercial laser communication solutions. The main product under development is the P-100 laser communication terminal which is also the system used in the practical work of this thesis.

3.2 P-100 laser communication terminal

3.2.1 Operating principles

The P-100 is a free-space laser communication terminal that is being developed by Cucuyo GmbH. The P-100 is designed to be an off-the-shelf communication terminal for different types of UAV platforms.The terminal is intended to be used as an alternative to the traditional RF communications whenever higher data rates or more secure transmissions are required. The P-100 terminal can be used for exchanging data between two or more UAVs or between a UAV and a ground station. The current design of the terminal is presented in Figure 1.

Figure 1: The current design of the P-100 laser communication terminal. (Image courtesy of Cucuyo GmbH.)

Aerial photography and videography are examples of typical UAV uses that require high data transfer rates to be successful. Typical missions that incorporate aerial photography in some form include search and rescue, aerial reconnaissance, infrastructure monitoring, and disaster management. All of these require or benefit from stable and fast transmissions of the captured images. A diagram of a generalised mission structure is presented in Figure 2.

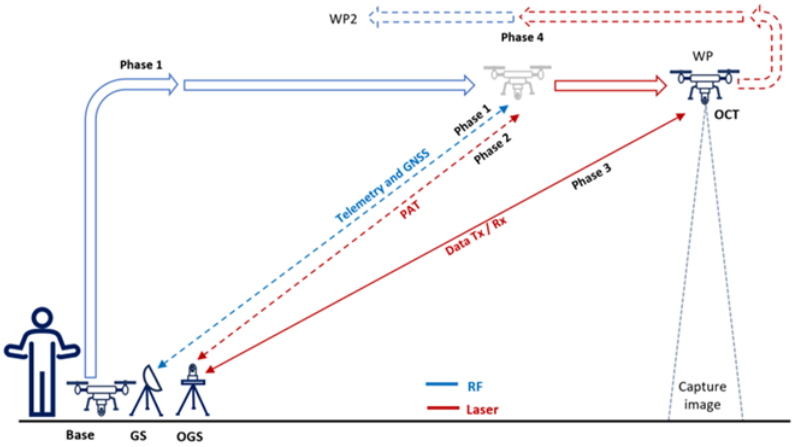

Figure 2: A typical UAV mission utilising the P-100 terminal. (Image courtesy of Cucuyo GmbH.)

The generalised mission structure is divided in four phases. In phase 1, the UAV starts moving towards the mission waypoint (WP) while sending its coordinates to the ground station (GS) via RF communications. The location data can be in the form of global navigation satellite system (GNSS) data. In phase 2, the pointing, acquisition and tracking (PAT) process is started between the optical ground station (OGS) and the optical communication terminal (OCT) of the UAV. The laser terminals of the UAV and the OGS use the coordinate data to point roughly at the direction of each other. Next, the first terminal initiates a spiral scan sequence to obtain the fine position of the second terminal. Both terminals perform spiral scans until the beams are locked in and a stable communication link has been established. Switching fully to laser communications marks the beginning of phase 3. In this phase, the UAV arrives to the waypoint and is ready to execute the mission task. Phase 3 concludes with the acquisition and transmission of the mission data to the OGS. The mission concludes with phase 4 in which the UAV either returns to base or moves to another waypoint. In phase 4, the laser link can again be supported by the RF communications if needed.

The generalised mission structure sets the performance requirements for the terminal and it is the foundation on which the system design is based. For the purposes of the thesis, the phase 3 is particularly important as it describes the PAT process. The PAT process describes the basic requirements for a successful laser communication link and the final control system should be able to perform the following three step process:

1. Point the terminal towards the target efficiently and with minimal error.

2. Acquire the signal from the target and fine tune the pointing angle to establish a communication link.

3. Track the target and maintain the communication link by compensating any movements and external disturbances.

3.2.2 Design of the terminal

The P-100 terminal operates by transmitting a modulated laser beam through its optical system and projecting it into free space. If the terminal is aligned properly with its counterpart, the beam is then transmitted through the receiving terminals optical system and demodulated to read the transmitted data. Properly aligning the laser beam requires a mechanism for steering the beam in space. The P-100 achieves this with the coarse pointing assembly (CPA) and the fine pointing assembly (FPA). Figure 3 illustrates the general optical path of the laser beam and how it can be altered with the CPA and the FPA.

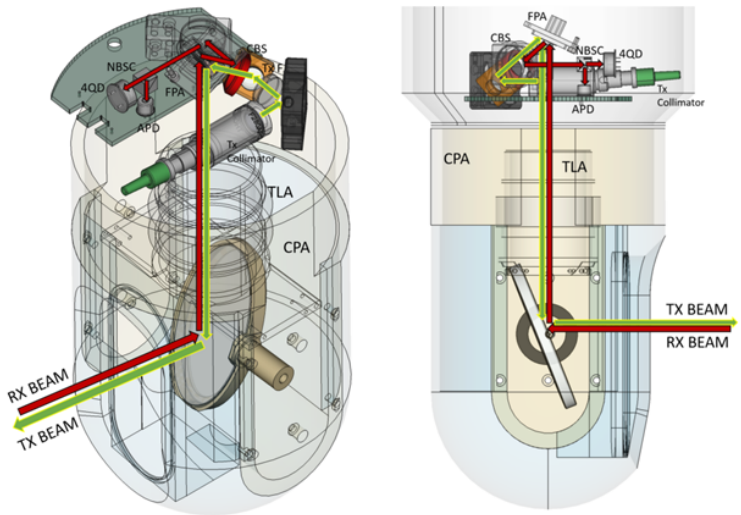

Figure 3: The optical path of the laser beam inside the P-100 terminal. (Image courtesy of Cucuyo GmbH.)

As seen in Figure 3, the transmit and receive signals mostly follow the same optical paths. The transmit beam is generated by a laser diode and it differs from the receive beam by its wavelength. This makes it possible to separate the two different beams by using a chromatic beam splitter (CBS). The CBS is placed right after the laser diode and a collimator, which lets the beam pass directly to the FPA. The FPA consists of a voltage controlled micro electromechanical system (MEMS) mirror, that can be used to deflect the beam by $\pm 1°$. After this, the beam goes through the telescope assembly (TLA) which expands the transmit beam. Finally, the transmit beam reaches the CPA which consists of an azimuth motor that rotates the whole assembly and an elevation mirror that can be used to steer the beam. With the combination of these two motors, it is possible to steer the beam $\pm 180°$ around the z-axis of the base and from $-45°$ to

+20° around the elevation mirror axis as depicted in Figure 4. It is important to note that the provided angles are optical angles. To obtain the mechanical angles for the elevation mirror, the optical elevation angle needs to be halved.

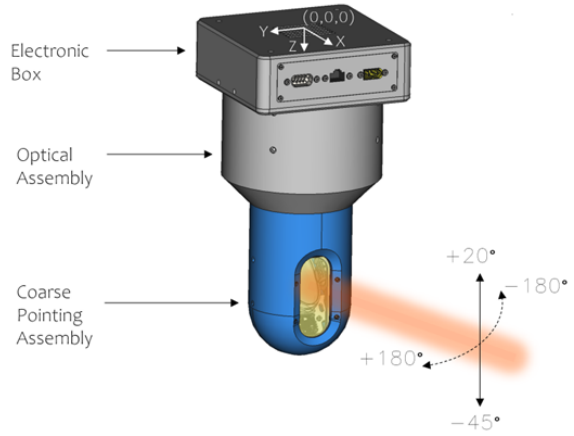

Figure 4: The base coordinate system and optical range of the CPA angles. (Image courtesy of Cucuyo GmbH.)

The receive beam follows the same optical path as the transmit beam until it reaches the CBS. From there the receive beam is deflected to a neutral beam splitter cube (NBSC) which splits the beam between the two detectors in the optical assembly, which are the avalanche photodiode (APD) and the four quadrant detector (4QD). The avalanche photodiode is used to collect the received signal and demodulate it to obtain the user data. The 4QD is used to track the position of the laser beam on the APD. The 4QD, as the name suggests, is split into four quadrants and the alignment of the beam can be calculated based on how the total beam intensity is spread across these four segments. This alignment data can then be used in a feedback loop to ensure alignment tracking after a laser communication link has been established. The 4QD detector data is mainly used by the FPA, but CPA can also access it directly, or through the movements of the FPA.

3.2.3 Coarse pointing assembly

The CPA of the P-100 terminal is essentially a 2-axis gimbal. The azimuth motor rotates the whole CPA around the z-axis of the base frame as demonstrated in Figure 4. The elevation motor on the other hand controls the angle around its own axis by rotating the elevation mirror. Both motors are frameless, hollow-shaft servo motors and both axes use absolute magnetic encoders to obtain position and velocity data. Both motors are also powered and controlled by Elmo Gold Solo Twitter servo drives, which are discussed more in depth in the next section. The stripped CPA with the elevation mirror and the Elmo drive can be seen in Figure 5

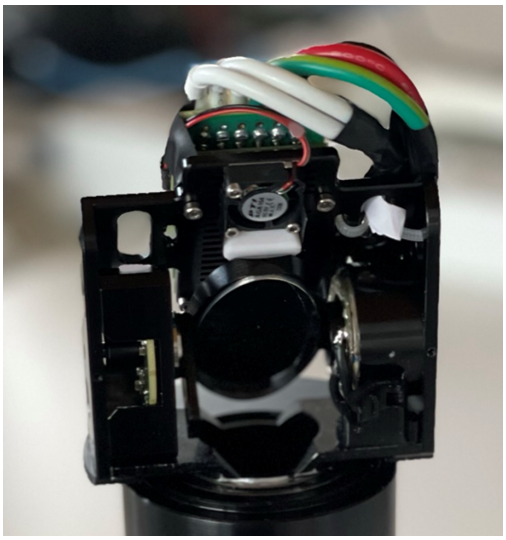

Figure 5: The coarse pointing assembly without the cabling and cover assembled. (Image courtesy of Cucuyo GmbH.)

There are a few key differences between the elevation and the azimuth assemblies with regards to their mechanical designs. Firstly, the elevation motor is very lightly loaded as it only needs to rotate the elevation mirror whose centre of mass can be aligned with the axis of rotation. However, the movement of the motor is restricted to approximately $\pm 30^{\circ}$ due to the mirror colliding with the elevation frame. On the other hand, the azimuth motor has much larger rotation angles but it also has to move the entire elevation assembly as seen in 5. The cables from the elevation motor are also coiled around the CPA and encased with protective cover.

3.2.4 Elmo motor drives

All of the 3-phase motors in the P-100 terminal are powered and controlled by Elmo Gold Solo Twitter servo drives[1]. The servo drives are not only used to drive the motors, but they also come with a motion processing unit that can be used to control the motors either by current, velocity or position commands. The Elmo drives also come with an Elmo Application studio II (EASII) software which provides the following tools for controller design:

- Automated process for identifying current and velocity plants for different motors.
- Automated process for designing and tuning current, velocity and position controllers with advanced filtering options.
- Encoder and feedback configuration.
- Motion control tools and scripting.
- Motion and signal recorder.

[1] https://www.elmomc.com/product/gold-solo-twitter/

4 System boundaries and scope

This section will briefly discuss the system boundaries and the scope of the model. Before modelling the system, the system boundaries have to be defined and the scope of the model has to be agreed on. The beginning of the section defines the physical components of the system that will be modelled. The section then concludes by introducing two major simplifications to the model to limit its scope.

For this thesis, we model the CPA of the P-100 laser communication terminal. The CPA in essence, is a 2-axis gimbal system. In this thesis, the physical system that is modelled includes the motors, motor drives and motor loads of the azimuth and elevation axes of the CPA. The motor load refers to any rigid body that is directly attached to and is driven by the motor. For the elevation motor, this means the elevation mirror and the elevation mirror frame. For the azimuth motor, this means the entire elevation assembly.

The scope of the model refers to how much detail is included in the system model. A 2-axis gimbal is a multiple-input multiple-output (MIMO) system, which means that the gimbal axes have coupled dynamics. For instance, the inputs to the elevation axis can produce non-zero outputs at the azimuth and vice versa. It is possible to take these coupling effects into account when modelling the system but this greatly adds to the model complexity. Another alternative is to consider the two axes decoupled to simplify the model. We chose the latter approach for this thesis as we estimate that the masses and accelerations of the gimbal axes will not cause major coupling effects due to the size of the terminal. We consider the possible coupling torques as external disturbances in our analysis. This is the first major simplification to limit the scope of the model.

The second simplification considers the brushless and frameless DC motors used in the system. For the purpose of this thesis, we will model the motors as regular DC motors. Focusing on modelling the different phases and electrical characteristics of a brushless DC motor offers limited benefits when the focus is on the mechanical dynamics of the system as was also concluded in [18].

5 System modelling and controller design

This section introduces the necessary theoretical concepts used in the practical work of the thesis. The topics cover modelling of physical systems and methods for analysing controller performance.

5.1 First principles modelling

First principles refers to creating a model based on physical laws and principles, and it is often a good starting point if the physical behaviour of the system is known, as is the case with a DC motor. It is often a good starting point to help understand the underlying system dynamics.

5.1.1 Modelling a DC motor

The dynamic behaviour of a DC motor can be separated in electrical and mechanical parts, both described by a first order differential equation. The electrical dynamics can be obtained by Kirchhoff's Voltage Law, which states that the applied voltage equals the voltage drop around a closed loop. For the DC motor armature circuit, this can be written as follows:

$$V = L\frac{dI}{dt} + RI - e_b,$$

where V is the applied voltage, L is the armature inductance, I is the armature current, R is the armature resistance, and e_b is the back electromotive force (EMF) in volts. The back EMF is proportional to the angular velocity of the motor, ω, and thus the equation can be written as:

$$V = L\frac{dI}{dt} + RI + K_e\omega.$$

The mechanical dynamics can be obtained from Newton's second law, which states that the torques acting on the system must equal the rate of change of the angular momentum. If the rotor has a moment of inertia J, we can then write:

$$J\frac{d\omega}{dt} = T_m - T_L,$$

where T_m is the motor torque and T_L is the load torque. The amount of torque produced by the motor is directly proportional to the current flowing though the armature circuit, and it relates to the armature current with the motor torque constant K_t. In SI units, the motor torque constant and back EMF constant have the same numerical value, and for the rest of this thesis, we will use K to refer to both. The load torque represents the external torques opposing the motion of the rotor. This can be due to attached loads, gears, pulleys, gravitational forces, or external disturbances to name a few. Often a friction model is added separately to the mechanical description of a DC motor. A simple way to describe the frictional effects is to relate the friction to the angular

velocity with the damping coefficient B. Finally, this gives us the following differential equations for a DC motor:

$$\frac{d\omega}{dt} = (KI - B\omega - T_L)/J \tag{1a}$$

$$\frac{dI}{dt} = (V - RI - K\omega)/L. \tag{1b}$$

5.1.2 Transfer function model

The two differential equations that we derived describe the complete dynamics of a DC motor. For further analysis, the differential equations are often converted into transfer functions that characterise the input-output relations of the system. The equations are first linearised and then converted to complex frequency domain or the s-domain by taking the Laplace transform:

$$sJ\omega(s) + B\omega(s) = KI(s) \tag{2a}$$

$$sLI(s) + RI(s) = V(s) - K\omega(s), \tag{2b}$$

where the constants are the same as in the differential equations (1), but the time dependent variables have been transformed to their s-domain counterparts. Rearranging (2a) allows us to relate the input current to the mechanical output of the motor:

$$\frac{\omega(s)}{I(s)} = \frac{K}{Js + B}. \tag{3}$$

Similarly, we can obtain the transfer function for the armature circuit by relating the input voltage to the output current:

$$\frac{I(s)}{V(s)} = \frac{1}{Ls + R}. \tag{4}$$

What makes the transfer function model so useful, is how different systems can be linked together with simple mathematics to form much more complex systems. Multiplying these two transfer functions together will give us the complete system model of the DC motor:

$$\frac{\omega(s)}{V(s)} = \frac{K}{(Js + B)(Ls + R) + K^2}. \tag{5}$$

Furthermore, these system models, or plants, can just as easily be connected to controllers and filters to manipulate their response to inputs and achieve the desired performance. This can also be done graphically with the help of block diagrams. Figure 6 shows a block diagram of a DC motor and its control logic built from multiple transfer function blocks. In the diagram, series connections correspond to multiplication of transfer functions, and parallel connections correspond to summations.

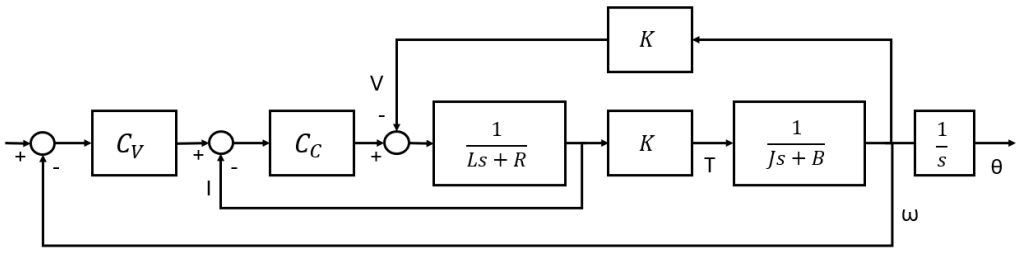

Figure 6: A block diagram of a DC motor with cascaded controllers. The outer controller is for the velocity and the inner controller is for the armature current. The integrator block at the end is used to obtain angles from the angular velocity.

5.1.3 State-space representation

Another alternative and commonly used representation for dynamic models is the state-space representation. In state space representation the system is described by the state vector $\mathbf{x}(t)$, the input vector $\mathbf{u}(t)$, and the output vector $\mathbf{y}(t)$. These vectors are related to each other with the state matrix $\mathbf{A}$, the input matrix $\mathbf{B}$, the output matrix $\mathbf{C}$, and the feedthrough matrix $\mathbf{D}$. It is a natural way of representing and analysing systems with multiple inputs and multiple outputs. The system equations are written as follows:

$$\dot{\mathbf{x}}(t) = \mathbf{A}\mathbf{x}(t) + \mathbf{B}\mathbf{u}(t) \tag{6a}$$
$$\mathbf{y}(t) = \mathbf{C}\mathbf{x}(t) + \mathbf{D}\mathbf{u}(t). \tag{6b}$$

By defining the state vector as $[\omega(t)\ I(t)]^T$ and the output vector as $\omega(t)$, using the DC motor equations (1) we can construct the state-space representation of the DC motor:

$$\begin{bmatrix} \dot{\omega}(t) \\ \dot{I}(t) \end{bmatrix} = \begin{bmatrix} -\frac{B}{J} & \frac{K}{J} \\ -\frac{K}{L} & -\frac{R}{L} \end{bmatrix} \begin{bmatrix} \omega(t) \\ I(t) \end{bmatrix} + \begin{bmatrix} 0 \\ \frac{1}{L} \end{bmatrix} V(t) \tag{7a}$$
$$\omega(t) = \begin{bmatrix} 1 & 0 \end{bmatrix} \begin{bmatrix} \omega(t) \\ I(t) \end{bmatrix}. \tag{7b}$$

5.2 System identification

This subsection will introduce the concept of system identification and black box modelling. The subsection starts by introducing the general concept of black box modelling. It then proceeds to analyse some excitation signal design concepts. The subsection ends with discussion on model fitting.

5.2.1 Black box modelling

Black box modelling refers to constructing a model of a system solely based on its input-output relations without knowledge of its internal dynamics or physics behind the process. The general black box modelling process starts by collecting input-output data of the system by feeding specific excitation signals through it. The data is then processed and used for fitting and validating models. Even though the model is chosen based on best correspondence to the collected data, good intuition and knowledge on the underlying dynamics can still help in choosing the best initial model. Constructing system models this way is an iterative process, and it uses the constant feedback and evaluation of the fit to refine the final system model.

5.2.2 Signal design

For any data to be collected, the system first has to be excited with appropriate signals. In their book on system identification, Pintelon and Schoukens discuss the importance of choosing the right excitation signal for optimal system identification and modelling [19]. Hardware limitations are an obvious consideration when it comes to choosing the signal to be used, but the type of the model also plays an important role in this choice. Linear and non-linear models require different excitation signal characteristics to be identified optimally. A system model used in simulations can differ from a system model used purely for controller design, and this can also be reflected in the system identification process. The main two parameters in the signal design are the frequency band that is excited and the amplitude of the excitation signal.

A sine wave is a simple signal to begin the identification process with and it can be implemented in most hardware. It can be used to detect non-linearities and to find resonance and anti-resonance points in the frequency domain. Sine waves can also be used to obtain the frequency response function of the system manually, but this is a very tedious and time consuming task. It is usually preferable to excite as many frequencies of interest at once as possible. A chirp signal is an excitation signal that quickly sweeps through a predetermined frequency range. It is a simple signal to generate and it offers an even excitation across the chosen frequencies and close to zero excitation on the frequencies outside the chosen range. The signal is also possible to implement in various hardware, as it does not require continuous movement and does not cause excess stress with abrupt changes in direction and magnitude. A multiphase multisine signal is a linear combination of multiple sinewaves with different phases and amplitudes. The signal offers even better energy distribution across the frequency range, and manipulating the even and odd phases allows for detection and estimation of non-linearities in the system [19]. However, this kind of signal is more difficult to create than a simple chirp signal, and hardware limitations might become a problem.

The excited frequency range and the magnitude of the excitation are just as important as the type of the signal. If chosen poorly, important characteristics of the system might not be captured or the system noise may be excited more than necessary, causing a poor noise-to-signal ratio. The frequency range should be chosen so that the system characteristics of interest lie within that range. Regarding the magnitude, Pintelon

and Schoukens recommend using low-amplitude signals when trying to extract the underlying linear systems and excitation signals representative of the real operating conditions when trying to achieve best linear approximation [19]. Understanding the mechanisms behind the system noise and disturbances helps in designing the appropriate signal, as it becomes clear at which frequencies and amplitudes the undesirable responses are pronounced.

5.2.3 Model fitting and validation

Fitting a model to data is an optimisation problem where we want to minimise the residuals by choosing the right parameters for the model. The process starts by choosing an initial guess for the model structure and computing the parameters using an optimisation algorithm such as least squares or maximum likelihood estimation. After obtaining the model parameters, the model is then validated and either accepted or rejected. If the model is rejected, the model structure is changed based on the observations and the procedure is then repeated.

There are many methods used in validating the fitted model. Most commonly, the model is used to simulate output, and the results are compared to the measured values from the real system. If the correspondence is high enough and all the important characteristics are captured, the model structure is accepted. A frequency response of the system is also often computed and compared with the frequency response of the real system. Other important methods include poles and zeros analysis and residual analysis. Ideally, the residuals should behave like white noise. Certain patterns in the residuals might be indicative of unmodelled dynamics, poor noise model, or feedback in the system, but the results should be analysed in the context of the used model and measurement setup [20].

The model structure will impact what kind of characteristics can be captured by the model. Models such as the transfer function model or the state-space model can be chosen to represent linear systems. Different polynomial models such as the output error or Box-Jenkins models are also used based on the noise characteristics of the system. Even though the black box modelling relies on the input-output data, good knowledge of the system will help in choosing the model structure and order. It is always a good idea to start with a simple model, and if the dynamics are too complex for the simple model, only then increase the order. With higher order models there is always a risk of overfitting, which causes the model to be fitted to the noise in the system and it can no longer be used to predict the system behaviour using other datasets.

5.3 Frequency domain analysis

This subsection discusses concepts in frequency domain analysis and controller design. The subsection begins by introducing two graphical representations of frequency response data used in the thesis. The end of the subsection introduces concepts in controller and filter design and evaluation.

5.3.1 Bode and Nichols plots

The two graphical representations of frequency response data used in this thesis are the Bode plot and the Nichols plot. Both plots can be used to analyse the system performance and to gain intuition on the system dynamics.

The bode plot is used to plot the magnitude and the phase as a function of frequency. The gain is usually displayed in decibels and the phase in degrees, both in their separate plots. Given a transfer function $G(s)$, the magnitude in decibels is given as $20\log_{10}|H|$, and the phase is given as $\arg(H)$. An example of the Bode plot of a second order system represented by the transfer function $\frac{10}{s^2+2s+10}$ can be seen in Figure 7.

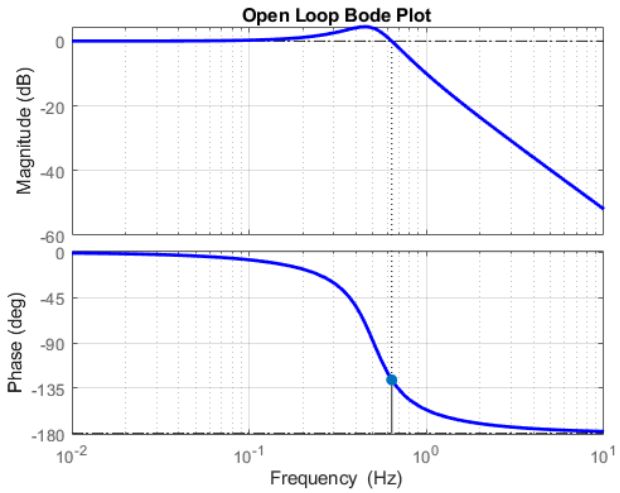

Figure 7: A Bode plot of a second order system.

The Nichols plot displays similar information to the Bode plot, but in the Nichols plot, both the phase and magnitude information can be found in the same plot. The Nichols plot displays the magnitude in decibels against the phase in degrees. It allows for easier analysis of the stability of the system, but the drawback is that there is no explicit frequency information displayed. The Nichols plot is also often plotted with constant magnitude and phase contour lines of the closed-loop transfer function with unity feedback. An example of the Nichols plot with the same second order system is shown in Figure 8

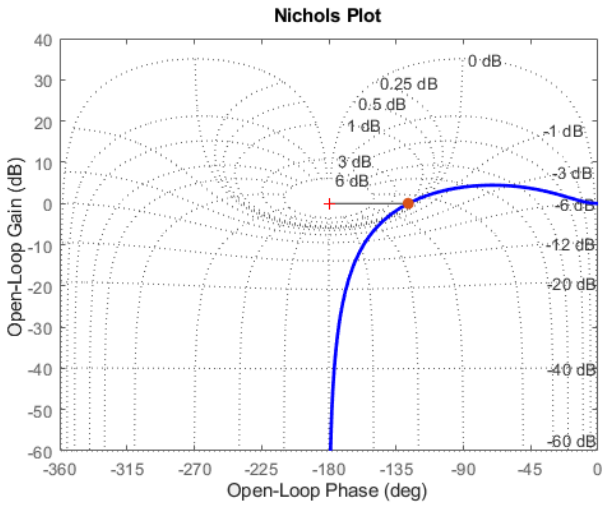

Figure 8: A Nichols plot of a second order system.

The Bode and Nichols plots can both be used to asses the stability of the controlled system by studying the gain and phase margins of the open-loop system. The gain margin refers to the amount of gain required to reach the unity gain at 0 dB at the frequency where the system phase reaches $-180°$. This frequency is also called the phase crossover frequency. On the other hand, the phase margin refers to the amount of phase shift required to reach the $-180°$ phase at the gain crossover frequency where the gain reaches 0 dB. There can be multiple crossover frequencies, but usually the smallest margins are used. The gain and phase margins describe how much shift in either pure phase or pure gain the system can tolerate before becoming unstable. In Figures 7 and 8, the phase margins are marked with the vertical and horizontal lines, and they have the value of approximately $53°$. The gain margins on the other hand are infinite, as the phase does not reach $-180°$. The simple gain and phase margins can be misleading, as they do not take into account the effect of varying both the gain and the margin simultaneously. The Nichols plot is slightly better in this aspect, as the graphical representation helps seeing the combined effect.

5.3.2 Controller and filter design

Poles and zeros are useful concepts in controller design and system stability analysis. They are most often used in the context of transfer functions, where poles refer to the values of the complex frequency s that make the denominator of the transfer function zero, and zeros refer to the values of s that make the numerator of the transfer function zero. Continuous time systems are deemed stable if all of the poles lie on the left-half of the complex s-plane. Discrete time systems on the other hand are stable if all of the poles lie within the unit circle on the s-plane.

Another important concept in controller design is the sensitivity function $S(s)$ and the complementary sensitivity function $T(s)$. The functions are described as follows:

$$S(s) = \frac{1}{1 + G(s)C(s)} \tag{8a}$$

$$T(s) = \frac{G(s)C(s)}{1 + G(s)C(s)}, \tag{8b}$$

where $G(s)$ is the system or plant transfer function and $C(s)$ is the controller transfer function. The closed-loop transfer function can be written as follows:

$$Y(s) = \frac{G(s)C(s)}{1 + G(s)C(s)}R(s) + \frac{1}{1 + G(s)C(s)}N(s), \tag{9}$$

where $Y(s)$ is the system output, $R(s)$ is the input reference, and $N(s)$ is noise added to the system at the plant output. From here it can be seen that the complementary sensitivity $T(s)$ describes how well the reference $R(s)$ can be tracked, but it also describes how robust the system is to high frequency noise and model uncertainty. The sensitivity $S(s)$ on the other hand describes how well the system can attenuate low frequency disturbances. When the magnitude of $S(s)$ is below 1, the disturbances at those frequencies are attenuated. When the values are above 1, the disturbances are amplified [15]. When designing controller, we would of course like to minimise both the sensitivity and the complementary sensitivity, but as the name suggests $S + T = 1$, which makes minimising both impossible. Designing a controller based on the sensitivity values is about balancing the two functions.

6 Modelling and designing a control system for the P-100 terminal

This section discusses the practical work of modelling and designing a control system for the CPA. The first subsection briefly describes the experimental setup used for measuring the dynamic behaviour of the system. The second subsection starts by building a first principles model of the system with the available information of the system. The third subsection focuses on input-output measurements, excitation signal design, and system identification. The fourth subsection uses the obtained models for frequency response analysis and controller design.

6.1 Experiment setup and preparation

The system used for the experimental work of the thesis is the P-100 laser communication terminal described in Section 3. The Elmo drives used to control the azimuth and elevation motors were connected to a laptop using RS-232 protocol. The motors were tuned using the EASII software. The software offers an automatic tuning procedure, where the current and velocity plants are identified, and current, velocity, and position controllers are designed automatically based on the identified models. Figure 9 shows a partial view of the controller design with the open-loop current plant. The current controllers are designed automatically based on the desired bandwidth and phase margin. The velocity and position controllers also allow for adjustable gain margin requirements.

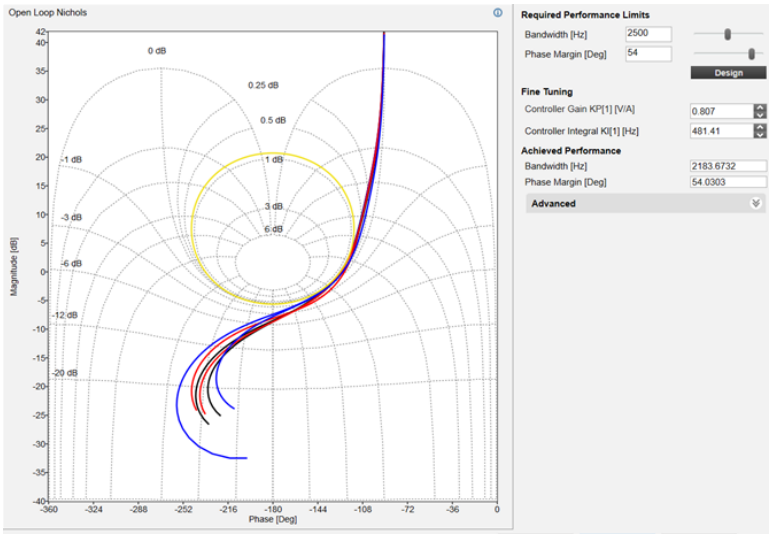

Figure 9: A current controller design view from the Elmo Application Studio II. The controller is designed automatically based on the bandwidth and phase margin requirements.

The software allows the user to save the frequency response data of the plants along with the controller and filter parameters. This data was collected after each tuning

procedure. However, the software does not allow the user to retrieve the identified model. The EASII software has extensive recording tools, which were used to collect data for the thesis. Unfortunately, recording data while sending commands to the motors would have required two different communication interfaces. A workaround was found by using the drive programming feature of the software. It is possible to upload user programs directly to the Elmo drive and then execute them in the drive while using the RS-232 protocol to transfer the recorded data. The effective sample time when executing the user programs had to be figured out, as it depends on the drive software background loop and the user program structure. The user program was made so that it first fills an empty array with the generated signal values and then proceeds to send the current commands specified by the values inside a for-loop. This structure itself adds some delay, as the instructions required by the loop structure need to be executed at each iteration. The sample time was calculated by sending 100 separate commands to form a one period of sinusoidal wave. As the period took 0.057 s to complete, it was concluded that the sample time for the specific program is 570 μs. The value was confirmed for each drive. Figure 10 shows the sample time measurement.

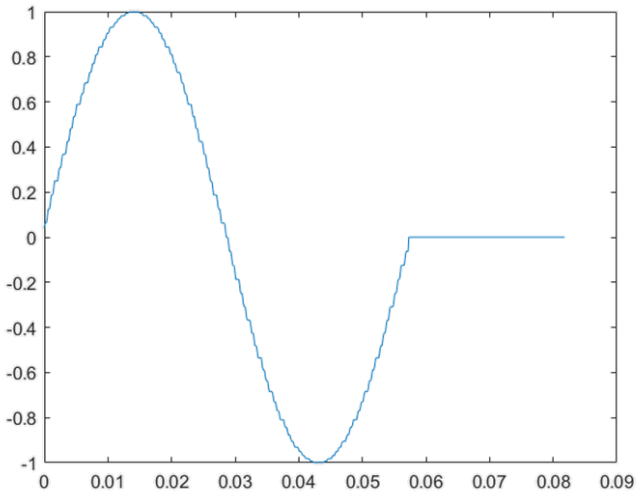

Figure 10: A sinusoid created using 100 commands to measure the sample time of the user program. It took 0.057 s to complete one period.

6.2 First principles model of the CPA

In this thesis, we start the modelling of the CPA with the first principles model of the system. It is a natural starting point and the process gives valuable insight into the system behaviour for further development.

The model is based on the boundaries and scope explained in section 4. It is always a good idea to start with a simple model and then build up complexity. We first apply the first principles model to the elevation axis, as its system dynamics should be much simpler than those of the azimuth axis. The elevation motor load is easier to measure

than its azimuth counterpart. The motor load consists of the elevation mirror and its frame, and their moments of inertia can be obtained from 3D models used for the design. The centre of mass of the elevation motor load can also be adjusted so that it lies on the axis of rotation. The azimuth motor has to move the entire elevation assembly, which might not be perfectly centered around its axis of rotation. In addition to this, the cabling from the elevation drive to the base of the terminal creates uneven resistance throughout the movement range of the motor. For these reasons alone, it is reasonable to begin by modelling only the elevation axis.

6.2.1 Model outline and parameters

The dynamics of the elevation axis can be described using the transfer function in (3). By using this model, we also assume that the current controller used by the Elmo drives is an ideal controller, which means that the active current of the motor at any given time is equal to the current command sent to the controller at that time. This is a reasonable assumption when the mechanical dynamics dominate in the system. The velocity plant is given as follows:

$$\frac{\omega(s)}{I_C(s)} = \frac{K}{Js + B},$$

where ω is the angular velocity of the motor, I_C is the current command to the motor, K is the torque constant, J is the combined moment of inertia of the motor and its load, and B is the viscous friction coefficient or the damping coefficient.

The viscous friction coefficient is used as a linear approximation of the damping effects found in the real system and it depends on the motor speed. It is used to group together all damping effects present in the system, such as frictional damping and electromagnetic damping. The damping coefficient is a constant, but it can also be non-linear due to the underlying physics. For instance, more complex non-linear friction models are often used to better capture the dynamics of the motor [21]. In the case of the elevation axis, the most prominent source of non-linearity seems to be the cogging torque, which is a periodic force resisting the movement of the motor caused by the permanent magnets of the motor. We an observe this as the motor locks to the magnetic field when rotated manually and without supplying any current.

6.2.2 Building the model

We obtained the torque constant and the moment of inertia of the motor from its datasheet [22]. We had to approximate the moment of inertia of the motor load based on the 3D model of the elevation mirror frame and by estimating the contribution of the mirror which was not included in the 3D model. The mirror is approximately the shape of the mirror frame, but because of its higher density relative to the frame, it is safe to assume that the order of its contribution is in the same magnitude or one magnitude larger. The estimated moments of inertia for the model are presented in table 1.

Table 1: The estimated moments of inertia.

Part	**J [kgm^2]**
Motor	$0.23 \cdot 10^{-6}$
Frame	$2.95 \cdot 10^{-6}$
Mirror	$3.00 \cdot 10^{-6}$–$30.00 \cdot 10^{-6}$
Total	$6.18 \cdot 10^{-6}$–$33.18 \cdot 10^{-6}$

The damping coefficient is harder to estimate in real systems. Assuming that in a steady state the torque produced by the motor is balanced out by the frictional and other damping effects proportional to the velocity, we obtain the balancing torque $T = B\omega$. This way, we can send a step current I to the motor, measure the input torque at steady state $T_{SS} = KI$ and divide it by the angular velocity at steady state ω_{SS} to obtain the damping coefficient B. This of course is a simplification of the real system dynamics and will give a very rough estimate. It is also not possible to achieve continuous rotation in all devices, as is the case with the fully assembled azimuth and elevation axes. During the assembly process, the elevation axis allowed for brief continuous rotation. However, the forces opposing the torque of the motor, such as the forces caused by the magnetic field of the permanent magnets and static friction, make it impossible to run the motor at low to moderate speeds without a velocity controller. The current needed to overcome the opposing forces is enough to quickly ramp up the motor to speeds that might cause damage to the assembly. At lower currents, it is possible to help the motor start its movement by pushing it manually, but the cogging torque causes oscillations at lower speeds. We were therefore not able to conduct any step response measurements reaching a steady state. However, we were able to measure a partial step response. The simulated step responses of the first principles model and the measured step responses of the real system are presented in Figure 11.

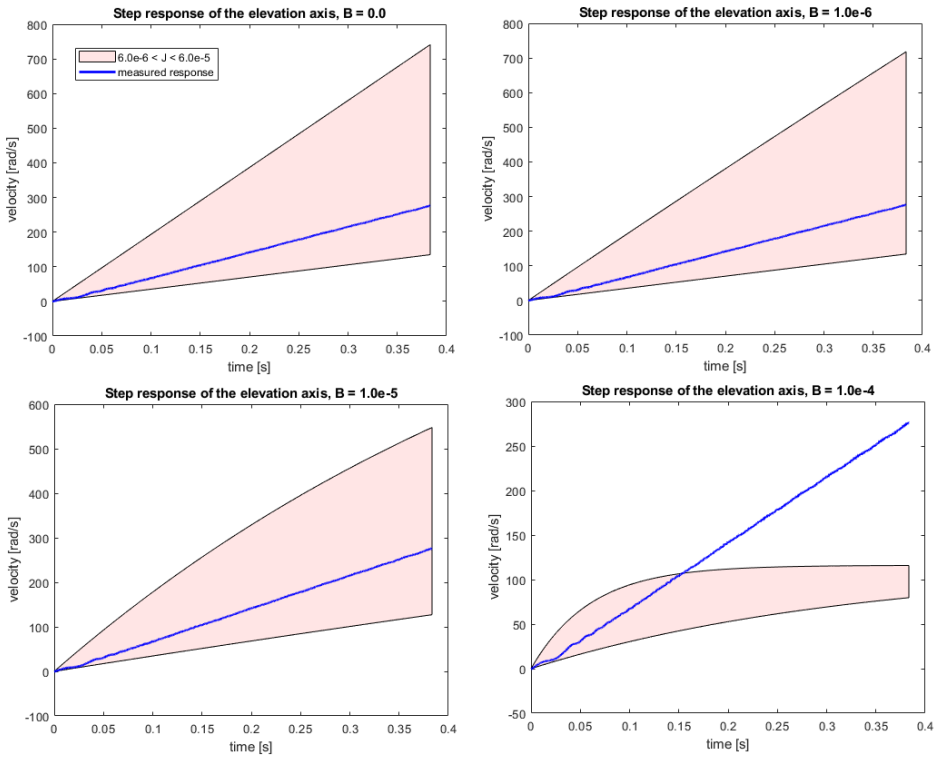

Figure 11: The partial step responses of the elevation axis. The blue line represents the actual measured response. The red filled area is the estimated motor load inertia. The different graphs are the same simulations performed with different magnitudes of the damping coefficient.

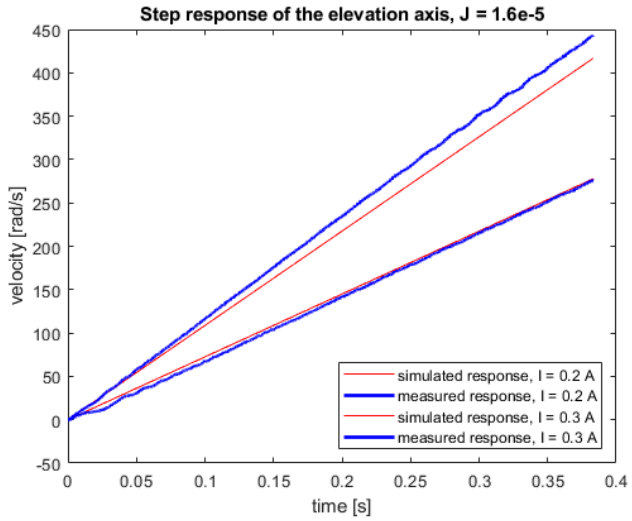

Figure 12: The partial step responses of the elevation axis. The blue line represents the actual measured response. The red line is the simulated response. The input current is varied while keeping the same model parameters.

As can be seen from Figure 11, small variances in the motor parameters can cause drastically different results and multiple parameter combinations can be used to achieve similar response. For the simulations in Figure 12, we considered the damping effects negligible and chose the motor load moment of inertia so that the simulated response best matches the measured response. We used the same motor parameters to simulate a response to a higher step current and compared the results to real measurements. It can be seen that the simulated response does not match the measured response anymore. This means that the simplified linear model fails to capture some key characteristics of the system. To improve the model, some of the parameters could be measured more accurately, for instance, the motor load, the damping coefficient and the static friction. The cogging torque could also be modelled as a non-linear periodic force. However, even with the simple elevation axis this quickly becomes a very complex task, especially for a system prototype that is bound to undergo multiple changes during its development. Some features are also not that easy to model, especially as the system complexity increases, as is the case when moving from the elevation axis to the azimuth axis.

The first principles model has revealed a lot about the system design and its dynamic behaviour. However, it is smarter to move on to other methods to obtain the mathematical description for the system. The next subsections will focus on identifying the system model using input-output measurements and designing a controller based on the identified model.

6.3 System identification of the CPA

This subsection describes the process of system identification and black box modelling of the CPA axes. The first half of the subsection discusses the excitation signal design and the data acquisition using the EASII software. The latter half focuses on system modelling in MATLAB.

6.3.1 Signal design and data acquisition

We designed the excitation signal for the input-output measurements using the principles introduced in Section 5.2.2. We chose a chirp signal because of its easy implementation and limitations both in the measurement system and the P-100 terminal. The drives have limited memory to store and execute user programs, which means that the excitation signal has to be fairly simple and easy to implement in just a few lines of code. The P-100 does not allow for continuous rotation when fully assembled, so for the most part, sending impulse or step signals to the motors was not possible. As mentioned in the beginning of this section, we discovered that the sample time of the user programs is 570 μs, which gives an approximate sampling frequency of 1750 Hz. We then calculated the Nyquist frequency to be at around 875 Hz, which is then the theoretical limit on the frequencies contained in the excitation signal. Realistically, the signals start to deteriorate before reaching this limit. Figures 13 and 14 show the spectrum of a 150 Hz and an 800 Hz excitation signals respectively.

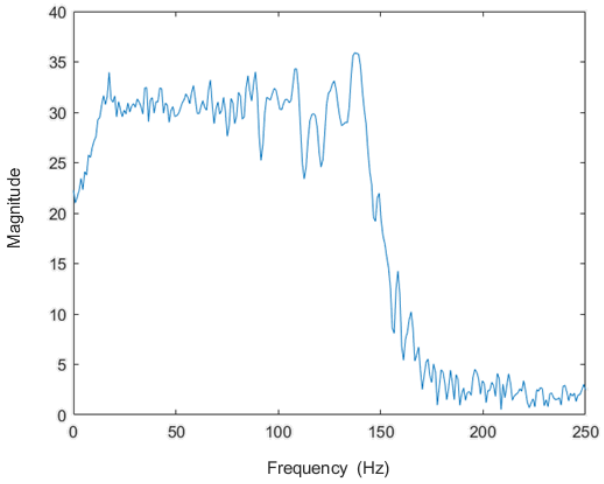

Figure 13: The Fourier transform of the 150 Hz chirp signal showing its spectral components.

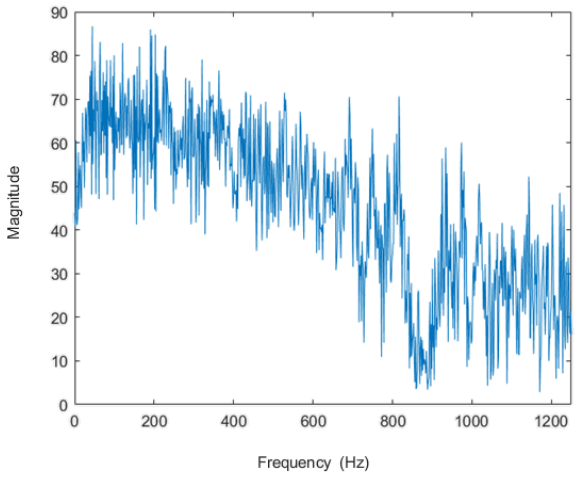

Figure 14: The Fourier transform of the 800 Hz chirp signal showing its spectral components.

We chose the 150 Hz chirp signal for all of the input-output measurements and conducted the experiments on both of the axes. The input signals had units of amperes as they were current commands sent to the controller. The resulting output was angular velocity in units of counts per second. We saved the data from two different terminals alongside the automatically identified plant frequency responses and the controller and filter parameters.

6.3.2 System identification

We started the system identification process by importing the collected data to MATLAB and seeing that we can replicate the Nichols plot from the EASII controller design page. We started by creating a transfer functions for the low-pass filter and PI controller using the saved parameters. This controller will be paired with all of the models that we examine in this section. The magnitude, phase, and frequency data were merged into a complex double datatype to capture the frequency response of the velocity plant. We also created a custom Nichols plot function that allows for more flexibility in plotting and troubleshooting. The resulting Nichols plot can be found in Figure 15.

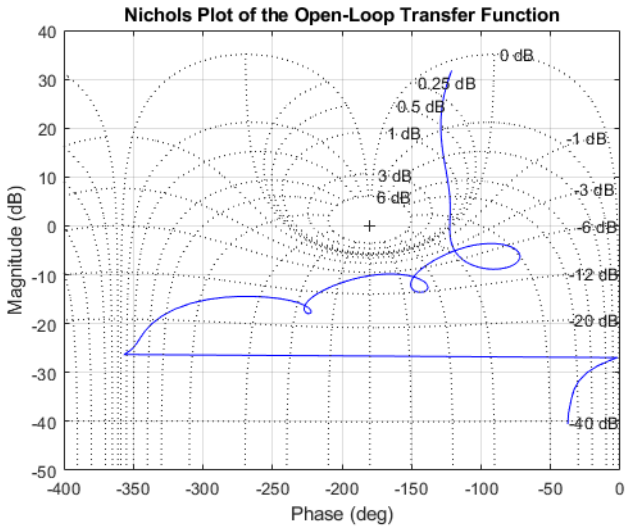

Figure 15: Frequency response of the azimuth axis model identified by EASII. Presented in a Nichols plot.

After importing the data to MATLAB, we created an iddata objects of all the measurements to make further analysis easier. En example of the input-output measurements can be seen in Figures 16 and 17.

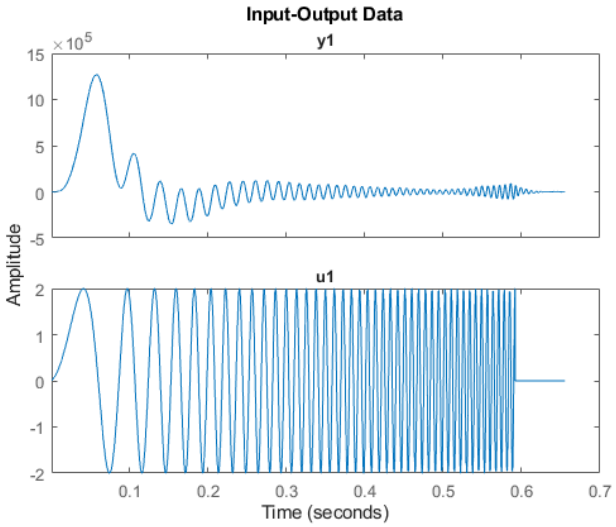

Figure 16: Input-output measurements of the system using a 150 Hz chirp signal, 1.5 A signal amplitude, and 200 μs measurement resolution.

The measurements performed with 1.5 amperes can be considered high amplitude excitations of the system. From the behaviour of the system, it can be concluded that there are high degrees of non-linearities present in the system. The initial velocities seem to be biased towards one direction, but the amplitude of the velocity output quickly fades as the input frequency increases.

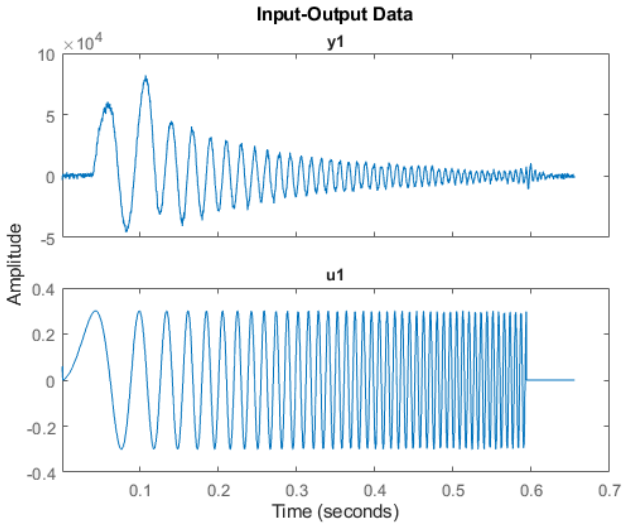

Figure 17: Input-output measurements of the system using a 150 Hz chirp signal, 0.3 A signal amplitude, and 200 μs measurement resolution.

The low amplitude measurements with 0.3 A produce different results. The behaviour of the system is closer to what could be expected from a chirp signal excitation. The velocity graph stays centered around the zero amplitude and there is

no clear bias present. In both cases the output amplitude quickly falls out, but sees an increase at the end of the signal.

We then used both signals to create transfer function and state space models of the system. The EASII software instructs using higher amplitudes for the identification of the systems, which would suggest that the software tries to find the best linear approximation to fit the data, rather than trying to extract the linear system [19]. We started the identification process with the high amplitude data as well, and found that the transfer function models could not replicate the results of the EASII software with any low order models. We then experimented with discrete time state-space models, and found out that the first order that gives comparable results is of the sixth order. Our assumption was, that as the DC motor model introduced in Section 5.1.3 is of the second order, a third or fourth order model would suffice. A fourth order continuous model captures the basic characteristics of the frequency response obtained from EASII, but we decided to not proceed with it as the model will be used to design a digital controller, which makes a discrete time model a more sensible choice. The system identification using the low amplitude data did not produce similar results to the model identified by EASII. Some of the Nichols plots obtained from the system identification are presented in Figures 19 and 18

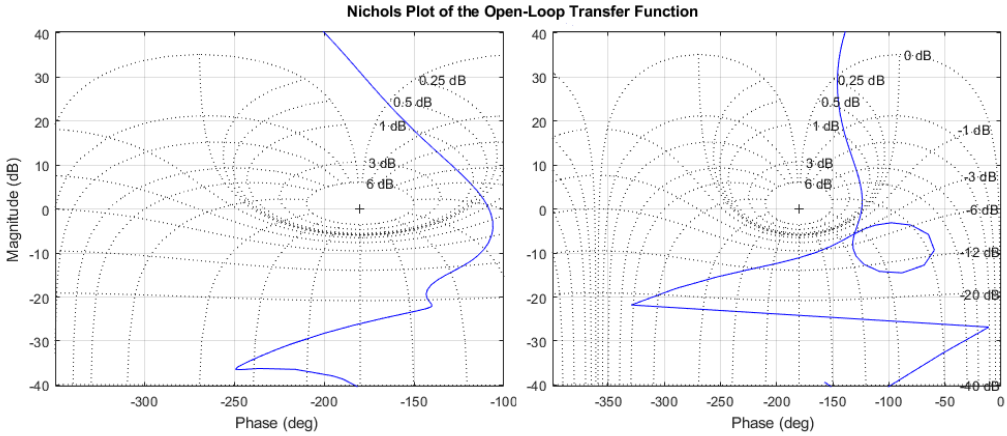

Figure 18: Frequency responses of two 6th order azimuth axis state-space models. Left to right: a discrete model fitted to low amplitude data and a discrete model fitted to high amplitude data.

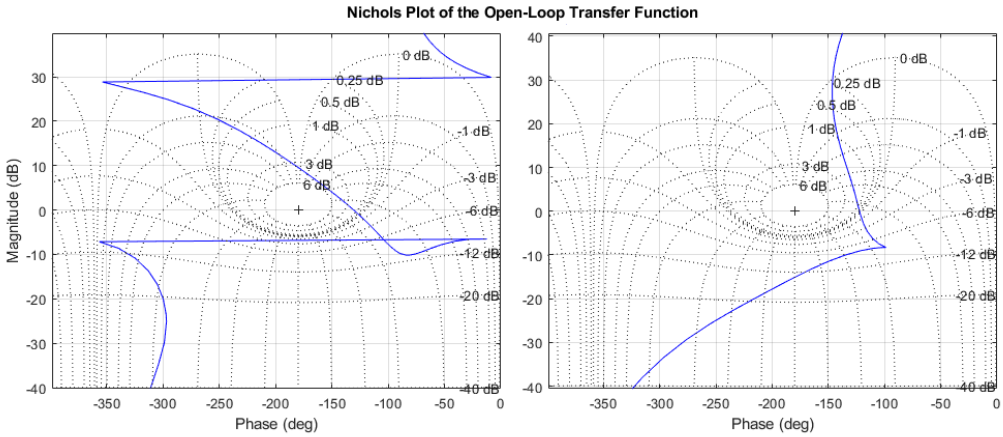

Figure 19: Frequency responses of two 4th order azimuth axis state-space models. Left to right: a discrete model fitted to high amplitude data and a continuous model fitted to high amplitude data.

Next we repeated the same procedure with the elevation axis. We found out that a third order model would already give satisfactory results with the elevation axis. This was expected as the elevation axis has less complexity in its design. The signal amplitude was again 1.5 A, which for the elevation motor is relatively much more higher current. The high amplitude signal also ensured that the cogging torque will not disturb the movement of the motor. The results of these measurements can be found in Figure 20.

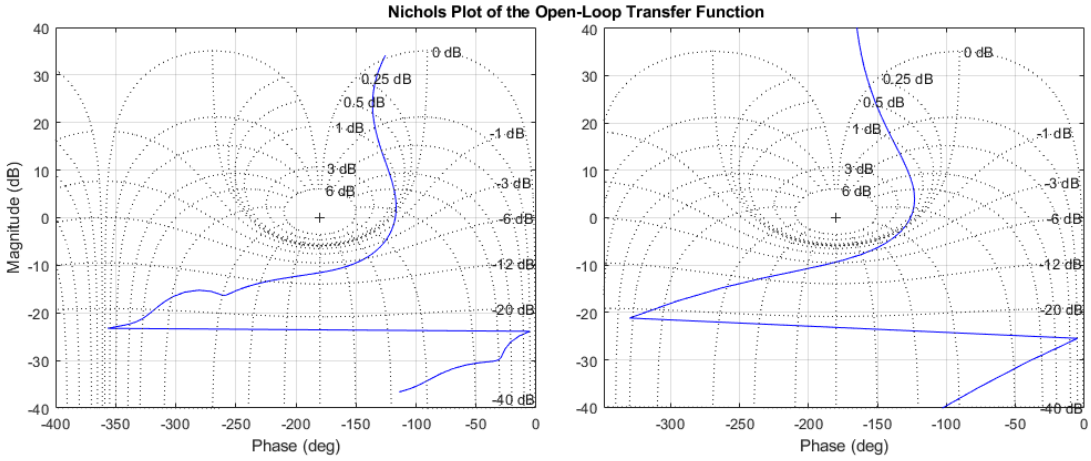

Figure 20: Comparison between the model identified by the EASII software and the 3rd order discrete state-space model fitted to input-output data.

After evaluating the frequency response data, we decided to continue with the third order state-space model for the elevation, and the sixth order state-space model for the azimuth axis. The next subsection will focus on controller design using the frequency domain data. The validation of the models will be done in Section 7.

6.4 Controller design with frequency domain data

This subsection will focus on controller design for the P-100 laser communication terminal using the previously identified models. We will now quickly go through the requirements for the controller

- The controller should achieve pointing with high accuracy.
- The controller should achieve a 50 μrad stabilisation together with the FPA.
- The controller should be able to perform the FPA offloading.

The Elmo drives have powerful motion processing units embedded in them and the tuning software for system identification and controller design. Based on our experience with the system, the pointing accuracy of the tuned system is not limited by the controller, but by the rotary encoders of the system. For the purposes of this thesis, the two last points are the most interesting ones. The stabilisation will be done using the velocity control loop. We will be basing our controller on the Elmo control logic, and see if it can be improved upon to better achieve the listed goals. The EASII software designs the control loops based on the gain and phase margins, but we will see if it is possible to implement our custom conditions when it comes to tuning the PI controller and selecting the filters. The Nichols plots of the identified models in Section 6.3.2 show that if we were to tune the controllers based on the same criteria of gain and phase margin, we would achieve similar tuning parameters. This is a good starting point, since we now know that using our model will yield similar tuning results as the model identified by EASII.

To make sure that the controller is tuned with the use of the P-100 terminal in mind, we want to include such tuning criteria that ensures it can perform well on a UAV platform in conjunction with the FPA. We then propose calculating the remaining disturbances by running the expected disturbance spectra through the combined system model sensitivity function, and tuning the controller based on the remaining in addition to the gain and phase margins. Unfortunately, modelling of the FPA was not in the scope of this thesis, and we did not obtain it in time for the analysis. However, we will still simulate the remaining error based on the expected disturbances. Publically available UAV flight data is scarce, but we were able to simulate expected disturbances based on the expected behaviour and a recent study on drone vibrations [23]. The final vibration spectrum comprises of quickly falling magnitude as the frequency increases, with a few resonant peaks at the levels suggested by the study. The magnitude units are arbitrary, as the paper describes linear accelerations in the UAV body, and we are interested in rotations of the optical head. The simulated disturbances can be found in Figure 21.

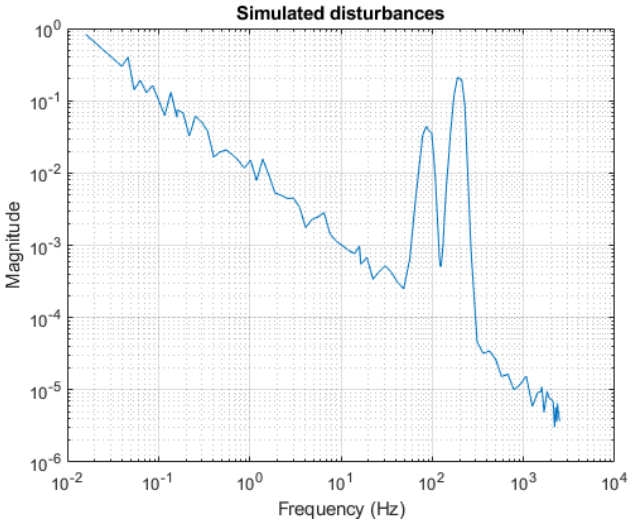

Figure 21: Expected UAV platform disturbances as a function of frequency. Magnitude in arbitrary units.

Next the sensitivity function was calculated for the azimuth axis based on (8a). The resulting sensitivity function is presented in Figure 22

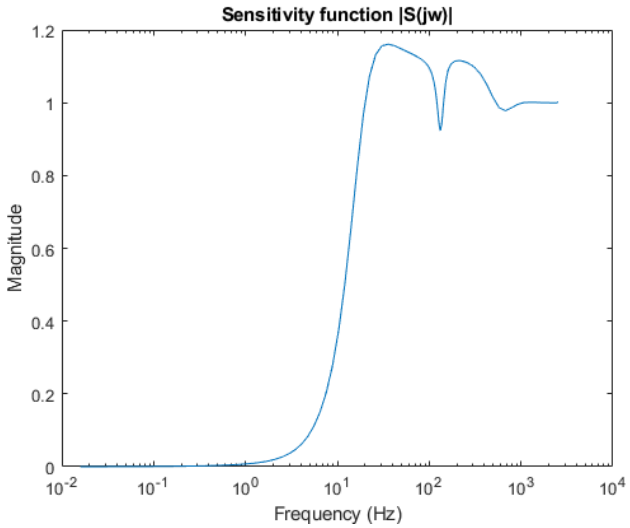

Figure 22: Sensitivity function of the azimuth axis.

We can notice that the sensitivity function seems to have amplification at the frequencies that are also pronounced in the UAV vibration spectrum. After calculating the remaining noise using (9), we notice that the controller is able to suppress the disturbances well, but as expected, there are peaks at the UAV resonance and sensitivity peak frequencies. The remaining disturbance is displayed in Figure 23.

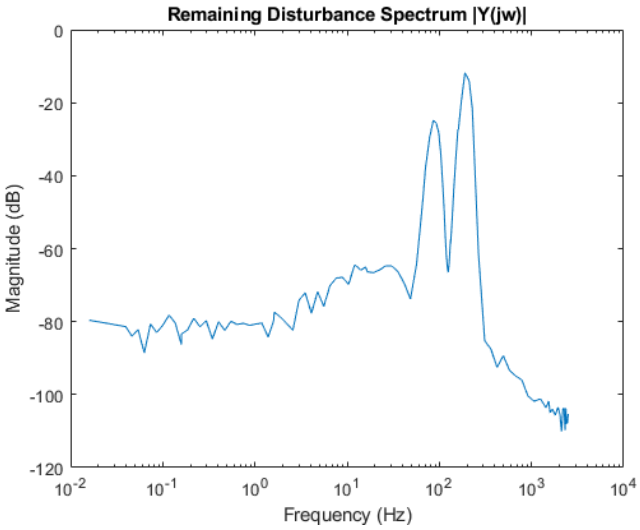

Figure 23: Remaining disturbance spectrum.

As the velocity controller is already tuned well, changing the controller parameters does not bring any additional benefits. The FPA operating range is up to 600 Hz, which could mean that the remaining disturbances are smoothed out when the combined system dynamics are used.

7 Evaluation and results

The system identification produced good results considering the limitations of the systems. However, the quality of the model beyond 150 Hz is not guaranteed, as the excitation band is cut off there. This happens to be just around the crossover frequencies depending on the model. This is easier to notice in the Bode plot as seen in Figure 24.

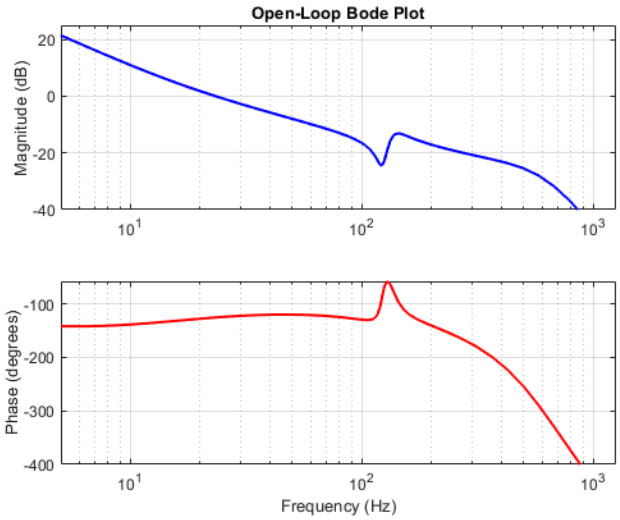

Figure 24: The open-loop bode plot of the azimuth model. The phase crossover frequency is at around 140 Hz.

The models that were obtained managed to replicate the frequency response of the EASII model very well. The behaviour was even closer with higher order models, but overfitting might become a problem if we only focus on replicating the EASII model. The models do not manage to produce simulation results comparable to the measured outputs. This was expected due to the non-linearities that are hard to capture in the model. An output comparison of the elevation axis is presented in Figure 25.

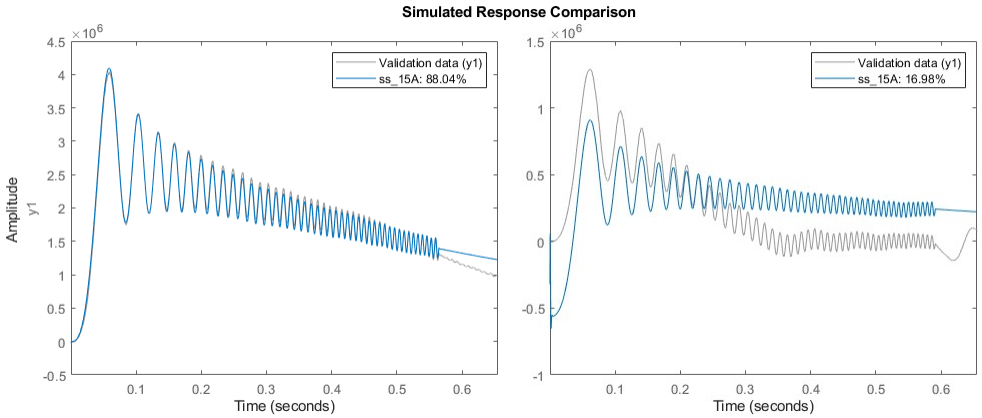

Figure 25: The simulated outputs of the elevation axis compared to the measured outputs. The comparison to training data is on the left and the comparison to validation data is on the right. The name ss_15A refers to state-space model with 1.5 A excitation signal.

Otherwise the software deems the models stable and proper. Looking at the poles and zeros maps, some models are marginally stable and show signs of noise and fitting issues. In Figure 26, the discrete time model poles stay inside the unit circle barely, and some poles and zeros are near cancelling each other. The residuals do not seem to indicate any problems.

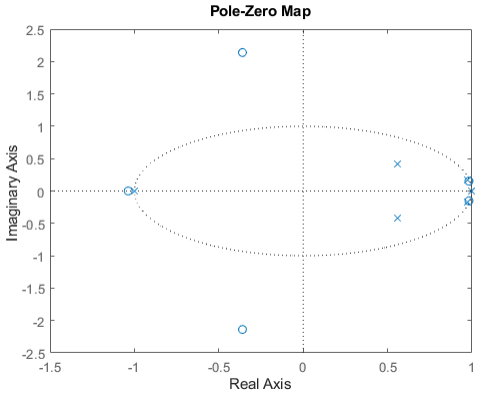

Figure 26: A 6th order discrete time model poles and zeros. The stability criterion requires all the poles to be inside the unit circle.

Overall the models seem to be good for their purpose of controller design. The model seems to be at least similar to the behaviour of the one that the EASII software uses for their controller design.

The controller performs as expected. Even though the disturbance spectrum is not measured from the target platforms, the estimated UAV disturbances offer a realistic scenario to test the rejection capabilities of the control system. The disturbances were attenuated well, except at the resonant peaks that also happened to coincide with the peak of the sensitivity function. The lower frequencies were attenuated well, which

indicates that the pointing and offloading goals should be achievable. The stabilisation depends on the combined CPA-FPA dynamics, which were not evaluated in the end.

8 Conclusions

The aim of the thesis was to model and design a control system for a laser communication terminal for UAV platforms that could achieve high accuracy pointing and stabilisation with effective disturbance rejection and robustness. A goal was also to create a repeatable and easy to implement procedure for modelling and designing control systems for similar systems.

We achieved the goal of modelling the P-100 laser communication terminal and tuning the controllers responsible for the azimuth and elevation axes. We validated our models by comparing them to the commercial software solutions used for the same purpose. We also proposed an alternative method for tuning the controllers, but we did not manage to test it due to missing system models of the target platform.

8.1 Future work

For future work we suggest refining the data acquisition process for the system identification. The chirp signal should be designed to span comfortably over the crossover frequencies, which are our points of interest in the frequency domain analysis. A rough sketch of the bode plot can be obtained with simple sine wave excitations if the crossover frequency locations are completely unknown.

Further analysis with the FPA model should be conducted to see if the proposed method of frequency response based tuning in conjunction with the FPA and UAV models would provide better results than the margin based tuning used in the EASII software.

References

[1] Z. Xiaoning, "Analysis of military application of uav swarm technology," in *2020 3rd International Conference on Unmanned Systems (ICUS)*. IEEE, 11 2020, pp. 1200–1204.

[2] H. S. Munawar, F. Ullah, S. Qayyum, S. I. Khan, and M. Mojtahedi, "Uavs in disaster management: Application of integrated aerial imagery and convolutional neural network for flood detection," *Sustainability*, vol. 13, p. 7547, 7 2021.

[3] A. M. Samad, N. Kamarulzaman, M. A. Hamdani, T. A. Mastor, and K. A. Hashim, "The potential of unmanned aerial vehicle (uav) for civilian and mapping application," in *2013 IEEE 3rd International Conference on System Engineering and Technology*. IEEE, 8 2013, pp. 313–318.

[4] H. Hemmati, *Near-earth laser communications, second edition*, 2nd ed. CRC Press, 2020.

[5] D. Forster, F. Goodwin, and W. Bridges, "Wide-band laser communications in space," *IEEE Journal of Quantum Electronics*, vol. 8, pp. 263–272, 2 1972.

[6] H. Kaushal, V. K. Jain, and S. Kar, *Free space optical communication*, 1st ed. Springer, 2017.

[7] J. M. Hilkert, "Inertially stabilized platform technology concepts and principles," *IEEE Control Systems*, vol. 28, pp. 26–46, 2 2008.

[8] M. Özçelik, B. Kürkçü, and Z. Y. Bayraktaroğlu, "Modelling and simulation of 2 dof gimbal system with experimental system identification," in *2022 10th International Conference on Systems and Control (ICSC)*. IEEE, 11 2022, pp. 508–515.

[9] W. Ren, Q. Qiao, K. Nie, and Y. Mao, "Robust dobc for stabilization loop of a two-axes gimbal system," *IEEE Access*, vol. 7, pp. 110 554–110 562, 2019.

[10] Q. Li, L. Liu, X. Ma, S.-L. Chen, H. Yun, and S. Tang, "Development of multitarget acquisition, pointing, and tracking system for airborne laser communication," *IEEE Transactions on Industrial Informatics*, vol. 15, pp. 1720–1729, 3 2019.

[11] Q. Duan, X. Zhou, Q. He, X. Chen, W. Liu, and Y. Mao, "Pointing control design based on the pid type-iii control loop for two-axis gimbal systems," *Sensors and Actuators A: Physical*, vol. 331, p. 112923, 11 2021.

[12] M. Pirzadeh and A. R. Toloei, "Design of generalized predictive control for the stabilizing loop from a two-axis gimbal seeker, considering cross-coupling in between two channels," *International Journal of Engineering*, vol. 32, 4 2019.

[13] C. Shen, S. Fan, X. Jiang, R. Tan, and D. Fan, "Dynamics modeling and theoretical study of the two-axis four-gimbal coarse–fine composite uav electro-optical pod," *Applied Sciences*, vol. 10, p. 1923, 3 2020.

[14] M. Borrello, "A multi stage pointing acquisition and tracking (pat) control system approach for air to air laser communications," in *Proceedings of the 2005, American Control Conference, 2005.* IEEE, 2005, pp. 3975–3980.

[15] K. J. Astrom and T. Hagglund, *PID controllers: Theory, design and tuning*, 2nd ed. ISA, 1995.

[16] D.-H. Lee, D.-Q. Tran, Y.-B. Kim, and S. Chakir, "A robust double active control system design for disturbance suppression of a two-axis gimbal system," *Electronics*, vol. 9, p. 1638, 10 2020.

[17] M. Baskin and K. Leblebicioğlu, "Combined system identification and robust control of a gimbal platform," *TURKISH JOURNAL OF ELECTRICAL ENGINEERING COMPUTER SCIENCES*, vol. 29, pp. 2247–2262, 7 2021.

[18] R. Y. Yamashita, F. L. Silva, F. M. Santiciolli, J. J. Eckert, F. G. Dedini, and L. C. A. Silva, "Comparison between two models of BLDC motor, simulation and data acquisition," *Journal of the Brazilian Society of Mechanical Sciences and Engineering*, vol. 40, p. 63, 2 2018.

[19] R. Pintelon and J. Schoukens, *System Identification: A Frequency Domain Approach*, 2nd ed., L. Hanzo, R. Abhari, J. Anderson, G. W. Arnold, F. Canavero, M. El-Hawary, B.-M. Haemmerli, M. Lanzerotti, D. Jacobson, O. P. Malik, S. Nahavandi, T. Samad, and G. Zobrist, Eds. John Wiley & Sons, Inc., 2012.

[20] L. Ljung, *System identification: Theory for the User*, 2nd ed., ser. Prentice Hall information and system sciences series. Philadelphia, PA: Prentice Hall, 12 1998.

[21] T. Tjahjowidodo, F. Al-Bender, and H. V. Brussel, "Friction identification and compensation in a dc motor," *IFAC Proceedings Volumes*, vol. 38, pp. 554–559, 1 2005.

[22] *Motor Parameters ILM25x08*, TQ-Systems GmbH, 2021, rev. 200.

[23] C. Ge, K. Dunno, M. A. Singh, L. Yuan, and L.-X. Lu, "Development of a drone's vibration, shock, and atmospheric profiles," *Applied Sciences*, vol. 11, p. 5176, 6 2021.